Spectroscopic factors and strength distributions for the deeply bound orbitals in ^{40}Ca obtained from the $(\vec{p},2p)$ reaction at 392 MeV

Y. Yasuda,[1,*] H. Sakaguchi,[1,†] S. Asaji,[2] K. Fujita,[3,‡] Y. Hagihara,[2] K. Hatanaka,[3] T. Ishida,[2] M. Itoh,[3,§] T. Kawabata,[4,∥]
S. Kishi,[1] T. Noro,[2] Y. Sakemi,[3,§] Y. Shimizu,[3,¶] H. Takeda,[5] Y. Tameshige,[3,**] S. Terashima,[1,††] M. Uchida,[3,‡‡] T. Wakasa,[2]
T. Yonemura,[2] H. P. Yoshida,[3,§] M. Yosoi,[3] and J. Zenihiro[1,†]

[1]*Department of Physics, Kyoto University, Kyoto 606-8502, Japan*
[2]*Department of Physics, Kyushu University, Fukuoka 812-8581, Japan*
[3]*Research Center for Nuclear Physics, Osaka University, Ibaraki, Osaka 567-0047, Japan*
[4]*Center for Nuclear Study, University of Tokyo, Wako, Saitama 351-0198, Japan*
[5]*RIKEN Nishina Center, Wako, Saitama 351-0198, Japan*

The cross sections and analyzing powers for the ^{40}Ca$(\vec{p},2p)$ reaction were measured. The strength distributions for the deep-hole states were obtained by a multipole decomposition analysis. The centroid energies and widths of the hole-state strengths of the $1p$ and $1s_{1/2}$ orbitals in ^{40}Ca were determined. The spectroscopic factors for the deeply bound $1p$ and $1s_{1/2}$ orbitals were extracted as $49 \pm 10\%$ and $78 \pm 14\%$ of the sum-rule limits of the independent-particle shell model, respectively. A strong influence of the nucleon-nucleon correlations on the spectroscopic factors is suggested.

I. INTRODUCTION

The independent-particle shell model (IPSM) in the nuclear mean field describes various nuclear-structure phenomena. However, the nucleon-nucleon (NN) correlations, which are not fully included in the mean field, cannot be ignored in a detailed study of the nucleus. The short-range correlations, which are related to the strong repulsive core of the NN interaction, are the most important of the NN correlations. Recently, the spin-isospin and tensor correlations have also received much attention because they play an important role in the binding of nucleons and affect the shell structure in exotic nuclei [1,2].

The spectroscopic factor is one of the important quantities indicating the influence of the NN correlations on the

———

*yusuke.yasuda@rcnp.osaka-u.ac.jp; present address: Research Center for Nuclear Physics, Osaka University, Ibaraki, Osaka 567-0047, Japan.

†Present address: Research Center for Nuclear Physics, Osaka University, Ibaraki, Osaka 567-0047, Japan.

‡Present address: Department of Physics, Kyushu University, Fukuoka 812-8581, Japan.

§Present address: Cyclotron and Radioisotope Center, Tohoku University, Sendai, Miyagi 980-8578, Japan.

∥Present address: Department of Physics, Kyoto University, Kyoto 606-8502, Japan.

¶Present address: RIKEN Nishina Center, Wako, Saitama 351-0198, Japan.

**Present address: Research Center for Charged Particle Therapy, National Institute of Radiological Sciences, Chiba 263-8555, Japan.

††Present address: GSI, Plankstrasse 1, D-64291 Darmstadt, Germany.

‡‡Present address: Department of Physics, Tokyo Institute of Technology, Tokyo 152-8550, Japan.

IPSM picture. In the $(e,e'p)$ experiments at the Nationaal Instituut voor Subatomaire Fysica, Amsterdam (NIKHEF), the spectroscopic factors for the nucleon orbitals close to the Fermi surface in several nuclei were reported to decrease to 60%–70% of the simple IPSM limits $(2J + 1)$ [3,4]. This reduction of the spectroscopic factor cannot be described in the IPSM. It was explained by Benhar *et al.* using a microscopic nuclear matter calculation with the correlated basis function (CBF) theory, including the NN correlations and surface effects [5]. Both the NN correlations and the surface effects contribute to the reduction of the hole-state strength near the Fermi surface, and the hole-state strengths were suggested to decrease to almost 80% of the IPSM limits far below the Fermi surface, where the surface effects are not important [5].

The spectroscopic factors calculated by Fabrocini *et al.* using CBF theory are quenched to 70% and 55% of the IPSM limits for the deepest $1s_{1/2}$ orbitals in ^{16}O and ^{40}Ca, respectively [6]. According to this calculation, the depletion of the spectroscopic factors by the NN correlations is 10%–15% for the valence orbitals and 30%–45% for the deeply bound orbitals. Most of the depletion was caused by the spin-isospin and tensor components of the NN correlations. Bisconti *et al.* calculated the spectroscopic factors for several doubly-closed-shell nuclei in a similar manner and predicted them to be 80% or more of the IPSM limits [7]. The spectroscopic factor for the deepest $1s_{1/2}$ orbital is suppressed owing to the NN correlations most strongly of all the orbitals in both of the calculations [6,7].

Since the $1s_{1/2}$ orbital is the deepest bound orbital far below the Fermi surface except for the very light nuclei, the spectroscopic factor for the $1s_{1/2}$ orbital will not be affected by surface effects but will be predominantly affected by the NN correlations. Therefore, it is important for a study of NN correlations to investigate the spectroscopic factor for the deeply bound $1s_{1/2}$ orbital in medium and heavy nuclei.

Single-particle properties such as spectroscopic factors and nucleon momentum distributions in a nucleus have long been studied experimentally by knockout reactions such as $(e,e'p)$ and $(p,2p)$ reactions [8–11]. Since ^{40}Ca is a doubly magic nucleus in the medium-mass region, many pioneering attempts have been made to examine the single-particle behavior of the deep-hole states by the $(e,e'p)$ [12–15] and $(p,2p)$ [16,17] reactions for ^{40}Ca. However, it was difficult to identify the hole state of the $1s_{1/2}$ orbital in the separation-energy spectrum because deep-hole states have large widths and overlap with adjacent hole states. The strengths for the deep-hole states were determined by fitting the measured recoil-momentum distribution of the cross section at each separation energy with the superposition of the knockout cross sections for a few orbitals calculated within the distorted-wave impulse approximation (DWIA) [12,14–17]. Mougey *et al.* presented spectroscopic factors of 75% of the IPSM limit for the $1s_{1/2}$ orbital and 95% for the $1p$ orbital [12]. Nakamura *et al.* reported spectroscopic factors for the $1s_{1/2}$ and $1p$ orbitals that are larger than the sum-rule limits [15]. Kullander *et al.* also obtained much larger spectroscopic factors [17]. The large spectroscopic factors in Refs. [15] and [17] are possibly caused by the small theoretical cross sections and contamination from other processes. As mentioned previously, the reported spectroscopic factors for the $1s_{1/2}$ orbital in ^{40}Ca are not consistent among the previous experiments, and this value of interest is still controversial.

In the 1990s, the Petersburg Nuclear Physics Institute (PNPI) group reported that they had succeeded in identifying the $1s_{1/2}$-hole states for medium- and heavy-mass nuclei such as ^{40}Ca, ^{90}Zr, and ^{208}Pb in the separation-energy spectra of $(p,2p)$ and (p,np) reactions with a proton beam at 1 GeV [18,19]. Since the absolute cross sections were not measured, the spectroscopic factors could not be given. However, these reports encouraged many researchers to study deep-hole states again.

The purpose of the present work is to identify deep-hole states and simultaneously deduce the spectroscopic factors for the deeply bound orbitals. For this purpose, the cross sections and analyzing powers for the ^{40}Ca$(p,2p)$ reaction were measured with a polarized proton beam at 392 MeV.

II. EXPERIMENTAL PROCEDURE

A. Kinematics

The separation energy is the energy required to knock out a proton from a target nucleus; it corresponds to the binding energy of the knocked-out proton. In the $A(p,2p)B$ reaction with a target nucleus A and a residual nucleus B, as illustrated in Fig. 1, the separation energy $E_{\rm sep}$ is given by

$$E_{\rm sep} = T_0 - T_1 - T_2 - T_3 = E_x - Q, \qquad (1)$$

where T_i $(i = 0, 1, 2, 3)$ are the kinetic energies of the incident proton $(i = 0)$, the scattered and knocked-out protons $(i = 1, 2)$, and the residual nucleus $(i = 3)$. The quantities E_x and Q indicate the excitation energy of the residual nucleus B and the reaction Q value [$Q = M_A - (M_B + m_p)$], respectively;
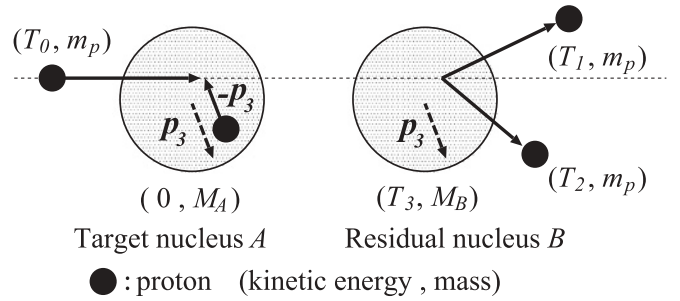

FIG. 1. Notation for the kinematics of the $A(p,2p)B$ reaction in the laboratory system. The incident energy of the proton is $T_0 = 392$ MeV in the present study. The recoil momentum of the residual nucleus B is indicated by p_3.

M_A, M_B, and m_p are the masses of the target nucleus, the residual nucleus, and the proton.

The momenta and the scattering angles of the two ejected protons were measured in the present $(p,2p)$ measurement. Although the residual nucleus was not detected, its recoil momentum ($\mathbf{p}_3$) was calculated from the momenta of the incident proton and two ejected protons on the basis of the momentum conservation law. Since the target nucleus is at rest, the proton ejected from it should have a momentum $-\mathbf{p}_3$ in the target nucleus before the scattering, if distortion is neglected.

B. Experimental setup

The experiment was performed at the Research Center for Nuclear Physics (RCNP), Osaka University, with a 392-MeV polarized proton beam accelerated by coupled cyclotrons. The proton beam from the polarized ion source was accelerated to an energy of 64.2 MeV by the azimuthally varying field (AVF) cyclotron and further accelerated to 392 MeV by the ring cyclotron [20]. The proton beam extracted from the ring cyclotron was achromatically transported to the target through the WS beamline [21].

The beam polarization was continuously monitored using a beamline polarimeter system with a polyethylene target. In the polarimeter system, kinematical coincidence was used to select p-H scattering from $({\rm CH_2})_n$ foil. Beam polarization of 60%–70% was achieved in the experiment.

The targets were two sheets of natural calcium foil with thicknesses of 53 and 24 mg/cm^2. The natural isotopic abundance of ^{40}Ca is 96.9% [22]. The oxygen contamination was estimated from elastic scattering and was less than 1% relative to calcium.

Scattered protons were analyzed with the dual-spectrometer system, the spectrometer Grand Raiden (GR) [23] and the large-acceptance spectrometer (LAS) [24]. A schematic view of the system is shown in Fig. 2. The GR was designed and constructed for high-resolution measurements with a resolution $p/\delta p = 37\,000$. This spectrometer consists of three dipole magnets (D1, D2, and DSR), two quadrupole magnets (Q1 and Q2), a sextupole magnet (SX), and a multipole magnet (MP). The third dipole magnet (DSR) required for in-plane polarization transfer measurements was not used in the present experiment. The LAS was designed to have a large solid angle ($\approx$20 msr) and a wide momentum acceptance ($\pm$15%) and
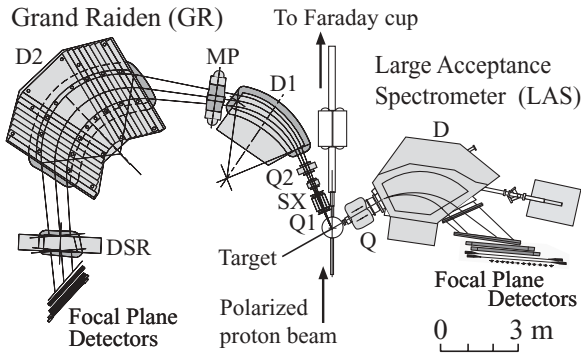
FIG. 2. Schematic view of the dual-arm spectrometer system at RCNP.

consists of a quadrupole (Q) and a dipole magnet (D). The two scattered protons were detected with the focal plane detectors in each spectrometer. Each focal plane detector consists of two plastic scintillation counters and two vertical-drift-type multiwire-drift chambers (VDCs); each chamber has two anode wire planes (X and U).

Two multiwire proportional chambers (MWPCs) were newly installed at the entrances of the GR and LAS to acquire the vertical-scattering-angle information, which cannot be precisely determined from measurements in the focal planes of the spectrometers owing to their ion-optical properties. The precise measurement of the scattering angles is important in calculating the recoil momentum of the residual nucleus. The MWPCs consist of two horizontal and two vertical wire planes whose wire pitch is 2.02 mm. The lead collimators were placed in front of the MWPCs for both the spectrometers. The layout around the scattering chamber is illustrated in Fig. 3. The solid angles of the GR and LAS were restricted to 1.5 and 15.5 msr, respectively, in the analysis software. However, when the LAS was set at 56.41°, its solid angle was decreased to 13.9 msr to eliminate pp scattering events.

After passing the target, the beam was transported into a Faraday cup in the shielding wall. The beam current collected
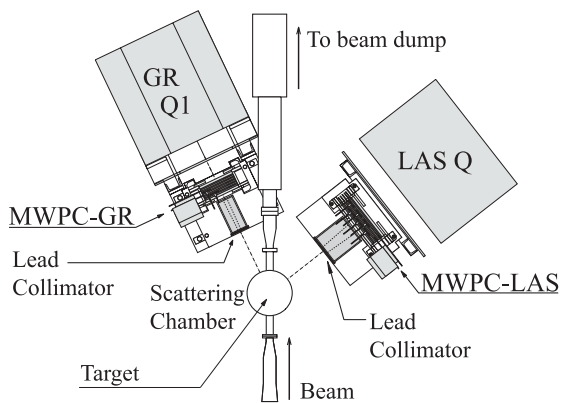

FIG. 3. Schematic view of the layout around the scattering chamber. The proton beam is injected into the reaction target at the center of the scattering chamber and is transported to a Faraday cup placed about 25 m downstream of the target. The MWPCs and the lead collimators are installed in front of the quadrupole magnets.

in the Faraday cup was monitored with a current digitizer (model 1000C) from Brookhaven Instruments Corporation. The data acquisition was initiated by the coincidence of the trigger signals from the GR and LAS scintillators.

C. Experimental conditions

As illustrated in Fig. 1 and mentioned in Sec. II A, the recoil momentum ($\mathbf{p}_3$) of the residual nucleus approximately reflects the Fermi momentum of the nucleon that is knocked out from the target nucleus owing to the momentum conservation law. Since the nucleon-momentum distribution in a nucleus is strongly related to the orbital angular momentum L, the recoil-momentum distribution of the cross section for the ($p,2p$) reaction predominantly depends on L. Because protons in the single-particle orbitals with $L \neq 0$ cannot have zero momentum in a nucleus, the cross sections for the knockout reaction from the single-particle orbitals with $L \neq 0$ should have a minimum around $p_3 = 0$. However, the cross sections of the s-hole states ($L = 0$) have a maximum at $p_3 = 0$.

To separate the hole states, the recoil-momentum distributions of the cross section and the analyzing power were measured in the region of 0–200 MeV/c in the separation energy region of 0–89 MeV. The angle of the GR was fixed at 25.5°. The magnetic fields of the spectrometers and the angle of the LAS were varied, while the sum of the kinetic energies of the two measured protons, $T_1 + T_2$, was kept constant at each separation energy. The experimental parameters are listed in Table I. The kinematical sets are grouped according to the range of the measured separation energies.

TABLE I. Measured kinematical sets (central values). The angle of the GR was fixed at 25.5°. θ_{LAS} indicates the angle of the LAS, which was set according to the measured separation-energy region.

	E_{sep} (MeV)		T_1 (MeV)	θ_{LAS} (deg)	T_2 (MeV)
Set 1	0–17	a	290.49	56.41	95.00
		b	270.20	56.41	115.29
		c	251.07	56.41	134.42
		d	233.22	56.41	152.27
Set 2	6–37	a	270.20	52.06	95.00
		b	251.07	52.06	114.13
		c	233.22	52.06	131.98
		d	218.25	52.06	146.95
Set 3	25–54	a	251.07	48.00	95.00
		b	233.22	48.00	112.85
		c	218.25	48.00	127.82
		d	203.70	48.00	142.37
Set 4	40–75	a	233.22	44.26	95.00
		b	218.25	44.26	109.97
		c	203.70	44.26	124.52
		d	189.00	44.26	139.22
Set 5	56–89	a	218.25	41.18	95.00
		b	203.70	41.18	109.55
		c	189.00	41.18	124.25
		d	175.00	41.18	138.25

III. DATA REDUCTION

Protons were identified by the ΔE signals of the plastic scintillators. The momenta and the horizontal scattering angles of the protons in the focal planes were obtained from their positions and angles measured by the VDCs. The vertical scattering angles were measured by the MWPCs at the entrances of the spectrometers. The momentum of the residual nucleus was calculated using the momentum conservation law. The separation energy was obtained via Eq. (1).

The proton beam from the cyclotron has a time structure with an approximately 60-ns period between bunches. To estimate the yield of accidental events, coincidence between the signals of the GR and LAS from adjacent beam bunches was allowed by increase in the width of the trigger signal of the GR. The yield of the true $(p,2p)$ events, which must originate from the same beam bunch, was estimated by subtracting the yield of the accidental events from the yield of the coincident events in the same beam bunch.

To determine the absolute cross sections, pp scattering was measured at $25.5°$ for the GR and at $60.0°$ for the LAS with 9.2 mg/cm^2 polyethylene targets. The uncertainties of the angle settings for the GR and LAS are less than $0.1°$. Since the solid angle and the momentum acceptance of the LAS are larger than those of the GR, the acceptance of the pp scattering measurement was determined by the GR. The measured cross section of pp scattering was 16.08 ± 0.18 mb/sr, which is consistent with the SAID [25] calculation value of 15.89 mb/sr within the measurement uncertainty. The analyzing power A_y of pp scattering was 0.340 ± 0.008, which differs by 6.6% from the SAID calculation value of $A_y = 0.364$. By addition of the systematic uncertainties to require a reduced χ^2 value of 1 in the comparison between the measured data and SAID values, the systematic uncertainties were estimated to be 2.0% for the cross section and 2.7% for the analyzing power. In the experiment with the calcium target, the uncertainty of 6% from the thickness of the calcium foil was included in the systematic uncertainty.

IV. DISTORTED-WAVE IMPULSE APPROXIMATION CALCULATION

The cross sections and analyzing powers were calculated for the $^{40}\text{Ca}(p,2p)^{39}\text{K}$ reaction using the DWIA code THREEDEE [26]. The NN scattering t matrix was taken from the solution of Arndt's phase-shift analysis [27]. The distorted waves were calculated using the Schrödinger equivalent potential from the Dirac global optical model parameters obtained by Cooper *et al.* [28]. The EDAD-1 potential parameter set was used in the calculations. The wave functions for the bound nucleons were calculated by adjusting the depth of the Woods-Saxon potential to reproduce the empirical separation energies. The parameters provided by Elton and Swift [29] were employed for the Woods-Saxon potential: $r_0 = 1.30$ fm, $a = 0.60$ fm, and $r_c = 1.25$ fm. Since the radius of the bound-state potential is critical for calculating the cross section, Elton's parameter choice was confirmed by evaluating the root-mean-square radius (RMSR) of the potential expected from the point nucleon distribution in the nucleus as follows.

The mean-square radius (MSR) of the charge distribution of the nucleus $\langle r_{\text{ch}}^2 \rangle$ can be written as

$$\langle r_{\text{ch}}^2 \rangle = \langle r_p^2 \rangle + \langle r_{\text{ch}}^2 \rangle_p + \frac{N}{Z} \langle r_{\text{ch}}^2 \rangle_n, \qquad (2)$$

where $\langle r_p^2 \rangle$, $\langle r_{\text{ch}}^2 \rangle_p$, and $\langle r_{\text{ch}}^2 \rangle_n$ denote the MSRs of the point proton distribution in the nucleus, the charge distribution of the proton, and the charge distribution of the neutron, respectively. Z and N indicate the number of protons and neutrons in the nucleus. The RMSRs of the charge distribution of the proton and of the ^{40}Ca nucleus are $\langle r_{\text{ch}}^2 \rangle_p^{1/2} = 0.8791$ fm [30] and $\langle r_{\text{ch}}^2 \rangle_{\text{Ca}}^{1/2} = 3.4764$ fm [30], respectively. The MSR of the neutron charge distribution, $\langle r_{\text{ch}}^2 \rangle_n$, is -0.1149 fm^2 [30]. Note that the negative value of $\langle r_{\text{ch}}^2 \rangle_n$ comes from the negative charge distribution in the larger-radius region of the neutron. From Eq. (2), the RMSR of the proton distribution in the ^{40}Ca nucleus is estimated as

$$\langle r_p^2 \rangle^{1/2} = \left(\langle r_{\text{ch}}^2 \rangle_{\text{Ca}} - \langle r_{\text{ch}}^2 \rangle_p - \frac{N}{Z} \langle r_{\text{ch}}^2 \rangle_n \right)^{1/2} = 3.38 \text{ fm.} \qquad (3)$$

The MSR of the potential in the nucleus can be considered as the sum of the MSR of the nucleon distribution in the nucleus and that of the NN interaction range. Assuming the effective interaction range of $\langle r_{\text{int}}^2 \rangle = 5.78$ fm^2 calculated from the mass-number-dependent formula $\langle r_{\text{int}}^2 \rangle = (0.132 \pm 0.013)A^{2/3} + (4.24 \pm 0.24)$ fm^2 [31], we evaluate the RMSR of the ^{40}Ca potential as

$$\langle r_{\text{pot}}^2 \rangle_{\text{Ca}}^{1/2} = \left[\langle r_p^2 \rangle + \langle r_{\text{int}}^2 \rangle \right]^{1/2} = 4.15 \text{ fm.} \qquad (4)$$

The MSR of the proton distribution is used instead of the MSR of the nucleon distribution because ^{40}Ca has the same number of protons and neutrons. It was confirmed that the RMSR of 4.14 fm for the Woods-Saxon potential with the Elton parameter is in good agreement with the estimated RMSR of 4.15 fm for the ^{40}Ca potential expected from the point nucleon distribution.

To compare the measured and calculated cross sections, the cross sections calculated with the DWIA code were averaged over the angular and momentum acceptances of the spectrometers.

V. MULTIPOLE DECOMPOSITION ANALYSIS

Since the deep-hole states induced by nucleon knockout reactions from deeply bound orbitals stay far above the particle-decay threshold and have short lifetimes, these states have large widths and overlap each other. If we assume that the cross sections for different hole states do not interfere coherently with each other, the measured cross section can be described by the superposition of cross sections for different hole states by the $(p,2p)$ reaction. Since the recoil-momentum distribution of the $(p,2p)$ reaction cross section predominantly depends on L, a superposition of the cross sections for the $(p,2p)$ reaction from different L orbitals was used for a fitting to the experimental recoil-momentum distribution data. The single-particle-hole strength for each orbital was obtained by the fitting. This technique is known as l decomposition [32] or multipole decomposition analysis (MDA).

The momentum distribution of the cross section at a separation energy E_{sep} is written in terms of the $(p,2p)$ cross section $\sigma_\alpha^{DWIA}(E_{sep}, T_1)$ for the single-particle-hole state obtained from a DWIA calculation as follows:

$$\sigma^{calc}(E_{sep}, T_1) = \sum_\alpha S_\alpha(E_{sep})\sigma_\alpha^{DWIA}(E_{sep}, T_1), \quad (5)$$

where α indicates an occupied single-particle orbital in the nucleus, for example $\alpha = 2s_{1/2}, 1d_{5/2}$, etc. $S_\alpha(E_{sep})$ is the hole-state strength for the orbital α. The quantity $\sigma(E_{sep}, T_1)$ denotes the triple-differential cross section,

$$\sigma(E_{sep}, T_1) = \frac{d^3\sigma}{d\Omega_1 d\Omega_2 dT_1}, \quad (6)$$

where Ω_1, Ω_2, and T_1 represent the solid angles of the two spectrometers and the kinetic energy of one of the scattered protons, respectively.

The χ^2 value for fitting to the cross-section data is defined by

$$\chi^2 = \sum_i \left(\frac{\sigma^{expt}(E_{sep}, T_{1i}) - \sigma^{calc}(E_{sep}, T_{1i})}{\Delta\sigma(E_{sep}, T_{1i})} \right)^2, \quad (7)$$

where $\sigma^{expt}(E_{sep}, T_1)$ and $\Delta\sigma(E_{sep}, T_i)$ are the measured cross section and its uncertainty, including the statistical and the systematic uncertainties. The summation index i runs to the number of data, and the S_α's were searched to minimize the χ^2 at each separation energy. The uncertainties in the S_α's correspond to a change of 1 in χ^2 from the minimum value. The spectroscopic factor for the orbital α is given by summing the strengths as

$$S_\alpha = \sum_{E_{sep}} S_\alpha(E_{sep}). \quad (8)$$

VI. RESULTS

A. Discrete states

The separation-energy spectrum up to 20 MeV is shown in Fig. 4. Two prominent peaks are observed at 8.3 and 10.9 MeV. The typical separation-energy resolution is 750 keV at full
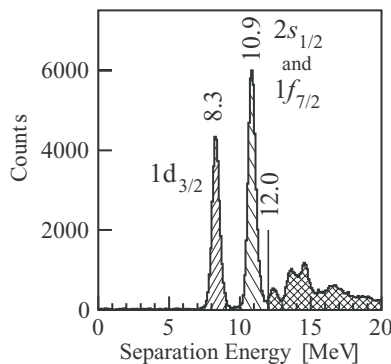

FIG. 4. Separation-energy spectrum of the ^{40}Ca$(p,2p)$ reaction up to $E_{sep} = 20$ MeV for kinematical set 1 (Table I). Two prominent peaks are observed at 8.3 and 10.9 MeV. The MDA was performed at separation energies above 12 MeV.
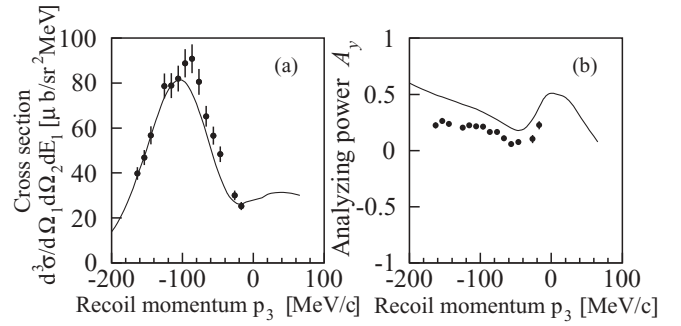

FIG. 5. Cross section (a) and analyzing power (b) of the ^{40}Ca$(p,2p)$ reaction for the peak at 8.3 MeV as functions of the recoil momentum p_3. The solid line represents the DWIA calculations fitted by the spectroscopic factor for the $1d_{3/2}$ orbital. The discrepancy in A_y (b) between the data and the DWIA calculation is discussed in the text (Sec. VI A).

width at half maximum (FWHM). The recoil-momentum distributions of the cross section and the analyzing power for these peaks are displayed in Figs. 5 and 6, respectively. The error bars represent the uncertainties, including the statistical and systematic uncertainties.

The first hole state is expected from a naive shell-model picture to be the hole state of the $1d_{3/2}$ orbital. In Fig. 5, the cross section has a minimum near $p_3 = 0$ MeV/c in the recoil-momentum distribution. This suggests that the peak consists of a hole state of a single-particle orbital with $L \neq 0$, as mentioned in Sec. II C. The solid curves in Fig. 5 show the recoil-momentum distributions for the hole state of the $1d_{3/2}$ orbital obtained from the DWIA calculation, which are normalized to the measured cross section. The DWIA calculation reproduces the measured cross section reasonably well. The calculation roughly reproduces the dependence of the recoil momentum on the analyzing power, but the value of the analyzing power is systematically overestimated in the entire recoil-momentum range. The spectroscopic factor deduced as the normalization factor is listed in Table II, together with the total and statistical uncertainties. The uncertainty that originates in the DWIA calculation was estimated in a similar

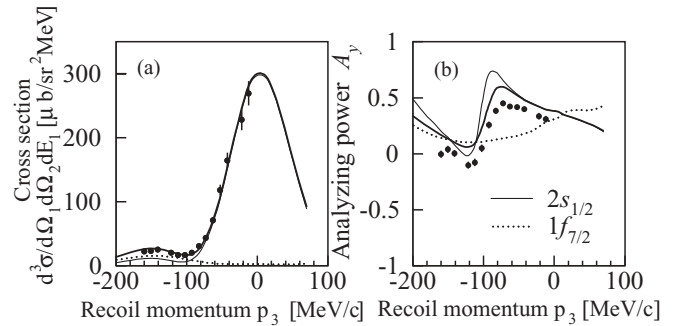FIG. 6. Results of the MDA for the peak at 10.9 MeV. The cross section (a) and the analyzing power (b) are shown as functions of the recoil momentum p_3. The thick solid line shows the fitted results. The thin solid line and the dotted line show the contributions of the $2s_{1/2}$ and $1f_{7/2}$ states, respectively. The discrepancy in A_y (b) between the data and the DWIA calculation is discussed in the text (Sec. VI A).

TABLE II. Spectroscopic factors for the discrete peaks in the ^{40}Ca measurement. Kramer *et al.* reanalyzed the previous $(d,^3\text{He})$ data of Doll *et al.* in Ref. [36] in their study [4]. For the present result, the first uncertainty is the total uncertainty, which includes the statistical uncertainty and the uncertainty from the DWIA calculation, and the second, in parentheses, is the statistical uncertainty included in the total.

	E_{sep} (MeV)	Orbital	Spectroscopic factor
Present work $(p,2p)$	8.3	$1d_{3/2}$	$3.12 \pm 0.53 (\pm 0.06)$
	10.9	$2s_{1/2}$	$1.01 \pm 0.17 (\pm 0.03)$
	10.9	$1f_{7/2}$	$0.78 \pm 0.14 (\pm 0.04)$
Kramer *et al.* [4]			
$(e,e'p)$	8.328	$1d_{3/2}$	2.58 ± 0.19
	10.850	$2s_{1/2}$	1.03 ± 0.07
$(d,^3\text{He})$ reanalysis	8.328	$1d_{3/2}$	2.30
	10.850	$2s_{1/2}$	1.03
Doll *et al.* [36]			
$(d,^3\text{He})$ $E_d = 52$ MeV	8.33	$1d_{3/2}$	3.70
	10.85	$2s_{1/2}$	1.65
	11.15	$1f_{7/2}$	0.58
$(d,^3\text{He})$ $E_d = 34.4$ MeV	8.33	$1d_{3/2}$	4.23
	10.85	$2s_{1/2}$	1.62
	11.15	$1f_{7/2}$	0.46

way in Ref. [33] by using other sets of input parameters for the DWIA calculation and evaluating the spectroscopic factors. The other parameter sets of Cooper *et al.* [28] and of Hama *et al.* [34] were used for the distorting potential, and the parameters provided by Sakaguchi *et al.* [31] and Kramer *et al.* [35] were employed for the Woods-Saxon potential. Through evaluation of the spectroscopic factors for the discrete peaks of the $1d_{3/2}$ orbital and the $2s_{1/2}$ and $1f_{7/2}$ orbitals, discussed in the following, the uncertainty owing to the distorting potential of 8% and that owing to the Woods-Saxon potential of 15% were found and added in quadrature for the total DWIA uncertainty. The uncertainty of 17% owing to the DWIA calculation was added in quadrature for the total uncertainty. The uncertainty outside the parentheses is the total uncertainty, and that inside parentheses means the statistical one included in the total.

In Fig. 6, the recoil-momentum distribution of the cross section for the peak at 10.9 MeV exhibits a maximum around 0 MeV/c, which is characteristic for a hole state of a single-particle orbital with $L = 0$. Therefore, the hole state of the $2s_{1/2}$ orbital is expected to be dominant in the peak at 10.9 MeV. Comparing with the level structure of ^{39}K [22], we see that the hole states of the $1f_{7/2}$ and $2p_{3/2}$ orbitals will be included in the peak as well. Since the contribution of the $2p_{3/2}$-hole state is negligible compared with those of the $2s_{1/2}$- and $1f_{7/2}$-hole states [36], the peak at 10.9 MeV was analyzed as the sum of the $2s_{1/2}$- and $1f_{7/2}$-hole states. We searched for the best set of normalization factors for the calculated cross sections for the $2s_{1/2}$- and $1f_{7/2}$-hole states to reproduce the measured cross sections. The result is shown in Fig. 6 and the spectroscopic factors obtained are listed in Table II. The fitted thick solid line for the cross section agrees well with the experimental data, but the calculated analyzing power is larger

than the measurement, which is similar to the results for the $1d_{3/2}$-hole state.

The spectroscopic factors for the valence orbitals were reported from the previous $(e,e'p)$ [4] and $(d,^3\text{He})$ [36] reactions as listed in Table II. The spectroscopic factors reported by Doll *et al.* from the $(d,^3\text{He})$ reaction are systematically larger than those from the $(e,e'p)$ reaction. However, Kramer *et al.* reanalyzed the same $(d,^3\text{He})$ data in Ref. [36] and showed that the spectroscopic factors for the $1d_{3/2}$ and $2s_{1/2}$ orbitals obtained from the $(e,e'p)$ and $(d,^3\text{He})$ experiments are consistent [4]. The spectroscopic factor for the $2s_{1/2}$ orbital obtained from the present study is in good agreement with the result in Ref. [4]; however, that for the $1d_{3/2}$ orbital is slightly larger than the result in Ref. [4].

Although the DWIA calculation describes the measured cross sections reasonably well, it systematically overestimates the analyzing powers, as seen in Figs. 5(b) and 6(b). The reduction of the analyzing power in exclusive measurements was previously observed and discussed by Noro *et al.* [37], Miller *et al.* [38], and Hatanaka *et al.* [39]. Furthermore, a similar reduction in the polarization P was observed by Miklukho *et al.* [40] and Andreev *et al.* [41]. These authors considered that the reduction might be caused by the influence of the effective mean density on the NN interaction. The systematic discrepancies between the experimental data and the DWIA calculation in Figs. 5(b) and 6(b) possibly imply the modification of the NN interaction in the nucleus. Although various extensive theoretical studies have been performed, no theoretical model has succeeded in reproducing the experimental analyzing power quantitatively.

The recoil-momentum distributions of the analyzing power are distinctive for different total angular momenta J of the orbitals, even if the corresponding orbital angular momenta L are the same. Therefore, the hole states induced from the orbitals with the total angular momenta $j_>$ and $j_<$ can be distinguished in principle by use of the analyzing power data. However, attempts to distinguish the hole states of the $j_>$ and $j_<$ orbitals in this way have unfortunately failed because the DWIA calculation of the analyzing power is not satisfactorily reliable. The results shown in the following sections are obtained from the MDA with the cross-section data only.

B. Broad-spectrum region at separation energies above 12 MeV

The MDA was performed for each 2-MeV bin in the separation energy region of 12–84 MeV. Since it was confirmed in the previous section that the DWIA calculation reproduces the measured cross sections reasonably well, the MDA with the cross-section data was able to reliably distinguish the hole state of the orbital with angular momentum L. The hole states of the $1s_{1/2}$, $2s_{1/2}$, $1p$, and $1d$ orbitals were taken into account in the MDA, since from the naive shell-model picture they are expected to dominate in the broad-spectrum region. As hole states of $j_>$ and $j_<$ orbitals with the same L cannot be distinguished in the present MDA, the single-particle-hole states were treated under the following assumptions.

The $1d$ orbital is split into the $1d_{3/2}$ and $1d_{5/2}$ orbitals by the spin-orbit interaction. Since the spectroscopic factor for the $1d_{3/2}$ orbital amounts to about 80% by the peak at 8.3 MeV,
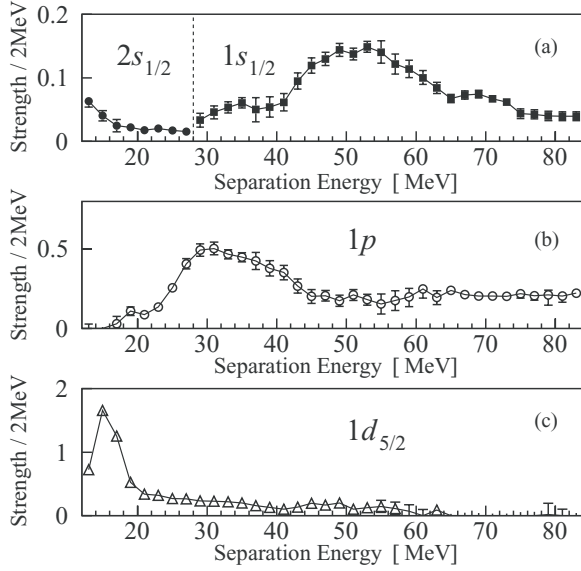
FIG. 7. Strength distributions obtained in the separation-energy region of 12–84 MeV. The solid lines are shown to guide the eyes. The vertical dotted line at 28 MeV in (a) shows the border where the s-hole state contribution was divided into the contribution of the $2s_{1/2}$-hole state and that of the $1s_{1/2}$-hole state.
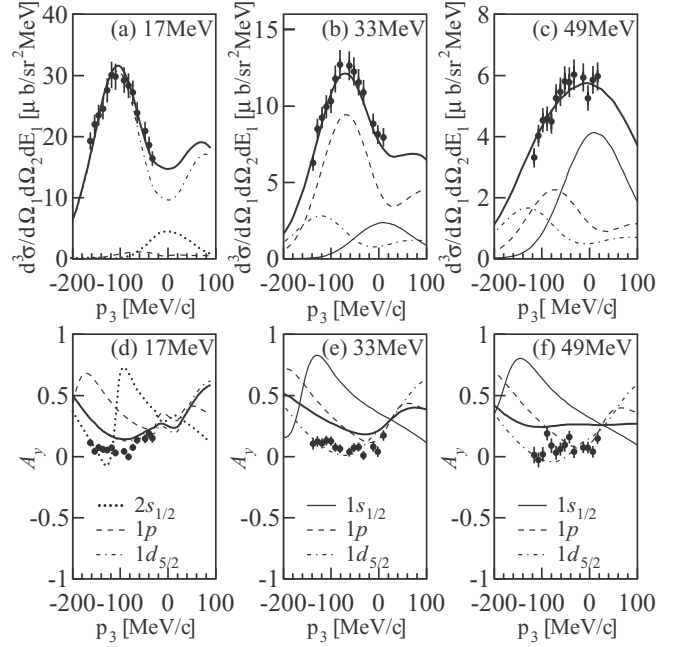

FIG. 8. Recoil-momentum dependence of the cross section and the analyzing power for the selected separation-energy bins at 17 [(a) and (d)], 33 [(b) and (e)], and 49 MeV [(c) and (f)]. The thick solid lines show the MDA results. The thin solid lines, the dotted lines, the short-dashed lines, and the dash-dotted lines show the contributions of the $1s_{1/2}$-, $2s_{1/2}$-, $1p$-, and $1d_{5/2}$-hole states, respectively.

the hole state of the $1d_{5/2}$ orbital is expected to dominate the d-state strength at separation energies above 12 MeV. The relative strengths for the $1p_{1/2}$- and $1p_{3/2}$-hole states were fixed in the ratio of 2:4, as suggested by the naive shell-model picture. Since the recoil-momentum distributions of the cross sections for the $1s_{1/2}$- and $2s_{1/2}$-hole states are quite similar, the strengths for the $1s_{1/2}$- and $2s_{1/2}$-hole states cannot be distinguished by the MDA. Therefore, the s-hole state strengths in the lower and higher separation-energy regions were assumed to be the strengths of the $2s_{1/2}$- and $1s_{1/2}$-hole states, respectively.

After use of the MDA, the hole states were separated by their orbital angular momentum L. Since the strength distribution obtained for the s-hole state has a minimum at 28 MeV, the s-hole state strengths were divided into the $2s_{1/2}$ and $1s_{1/2}$ strengths below and above 28 MeV. The strength distributions obtained for the $1s_{1/2}$-, $2s_{1/2}$-, $1p$-, and $1d_{5/2}$-hole states are shown in Fig. 7.

Figure 8 shows some examples of the fitted recoil-momentum distributions of the cross section and the analyzing power at separation energies of 17, 33, and 49 MeV. The fitted recoil-momentum distributions of the cross section reproduce reasonably well the measured cross-section data at each energy. It is found that the hole states of the $1d_{5/2}$, $1p$, and $1s_{1/2}$ orbitals are dominant in the cross sections at 17, 33, and 49 MeV, respectively. However, the calculated analyzing power shown in Figs. 8(d)–8(f) overestimates the experimental data at all of these energies, as mentioned in Sec. VI A.

The strength distributions obtained for the $1s_{1/2}$- and $1p$-hole states in Fig. 7 have hump structures at separation energies of 50 and 30 MeV, respectively. The continuum physical backgrounds are also observed in the strength distributions. Although the continuum strengths are appreciable

at separation energies larger than 80 MeV in the strength distributions for the $1s_{1/2}$- and $1p$-hole states, it is improbable that a single-particle-hole state has such a high separation energy. These strengths are probably contributions of many-body processes, such as $(p,3p)$ or $(p,2pn)$ reactions, or multistep processes that follow the knockout reactions.

In the $(p,3p)$ and $(p,2pn)$ reactions, the final states are four-body systems with the configurations of $3p + {}^{38}\text{Ar}$ and $2p + n + {}^{38}\text{K}$, respectively. The phase-space volumes of the four-body final states were considered under the condition that two protons in the final state were detected by the GR and LAS, but the other particles in the final states were not detected. The combined phase-space volume was obtained by averaging the phase-space volumes of the $(p,3p)$ and $(p,2pn)$ final states with equal weights. Since the ${}^{40}\text{Ca}(p,3p){}^{38}\text{Ar}$ and ${}^{40}\text{Ca}(p,2pn){}^{38}\text{K}$ reaction channels open at 14.7 and 21.4 MeV in the separation-energy spectrum, the combined phase-space volume increases from 14.7 MeV.

For the multistep processes, Cowley *et al.* studied the contribution of the rescattering processes that follow the knockout reactions to the coincidence measurement of the ${}^{40}\text{Ca}(p,2p)$ reaction [42]. The theoretical cross sections of an incoherent sum of the $(p,p'p'')$ and $(p,2p)$ reactions well reproduced their experimental coincidence spectra. The contributions of the rescattering processes that Cowley *et al.* calculated have shapes similar to the four-body phase space estimated here. Thus, we have used the estimated four-body phase space as the background-shape model, including the four-body and the
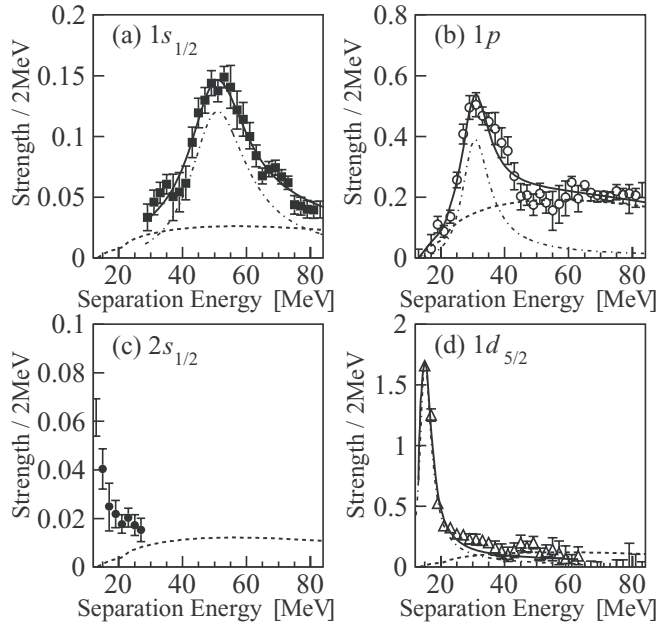
FIG. 9. Strength distributions for the hole states of the (a)$1s_{1/2}$, (b)$1p$, (c)$2s_{1/2}$, and (d)$1d_{5/2}$ orbitals in the separation energy region of 12–84 MeV. The solid lines and the dash-dotted lines in the figures for the $1s_{1/2}$-, $1p$-, and $1d_{5/2}$-hole states show the fitted curves and the fitted asymmetric Lorentzian functions, respectively. The short-dashed lines show the estimated contribution of the four-body background.

rescattering processes; the adequacy of the model will be discussed later.

An asymmetric Lorentzian shape was suggested by Sartor and Mahaux to describe the spectral function of a hole state near the particle threshold [43]. It can be written as

$$f(E_{\text{sep}}) = N \frac{1 + (E_{\text{sep}} - E_c)A}{(E_{\text{sep}} - E_c)^2 + \frac{1}{4}\Gamma^2}, \qquad (9)$$

where E_c and Γ are the centroid energy and width of the peak, and N and A are a normalization parameter and an asymmetric parameter. When the parameter A becomes small, the function becomes symmetric. We fitted a combination of the asymmetric Lorentzian function and the estimated phase-space volume to the strength distributions for the $1s_{1/2}$-, $1p$-, and $1d_{5/2}$-hole states. The background for the $2s_{1/2}$-hole state was determined to be of the same magnitude in the cross section as that for the $1s_{1/2}$-hole state. The dotted lines in Fig. 9 show the phase-space volumes that seem to give reasonable background shapes.

The reduced χ^2 of $\chi_\nu^2 = 0.92$ was obtained in the fit for the $1s_{1/2}$-hole state. The reduced χ^2 is defined as $\chi_\nu^2 = \chi^2/\nu$, where ν is the number of degrees of freedom in the fit. In the χ^2 fit for the $1p$- and $1d_{5/2}$-hole states, χ_ν^2 values of 1.3 and 1.7 were obtained, that is, they were larger than 1. If the model in the fit were perfect, χ_ν^2 would be 1. The larger χ_ν^2 is due to an inadequate model used in the fit. To compensate for this inadequacy of the model, the uncertainties in the parameters were estimated in the $1p$- and $1d_{5/2}$-hole state cases, following the method of Terashima *et al.* in Ref. [44]. The uncertainties in the strength data were artificially increased by multiplying

TABLE III. Centroid energies and widths (FWHM) of the strength distributions for the hole states of the $1p$ and $1s_{1/2}$ orbitals in ^{40}Ca. For the present result, the first uncertainty is the total uncertainty, which includes the statistical and the model uncertainties, and the second, in parentheses, is the statistical uncertainty included in the total.

		Centroid (MeV)	Width (MeV)
Present work	$1p$	$30.0 \pm 0.4 (\pm 0.3)$	$10.3 \pm 1.1 (\pm 0.9)$
$(p,2p)$	$1s_{1/2}$	$49.6 \pm 0.6 (\pm 0.6)$	$21.3 \pm 0.9 (\pm 0.9)$
Mougey *et al.*	$1p$	41	
$(e,e'p)$ [12]	$1s_{1/2}$	56	
Amaldi *et al.*[a]	$1p$	32 ± 4	18 ± 5
$(e,e'p)$ [13]	$1s_{1/2}$	77 ± 14	46 ± 24
Nakamura *et al.*[b]	$1p$	35 ± 1	21 ± 3
$(e,e'p)$ [15]	$1s_{1/2}$ (A)	58.7 ± 1.2	36 ± 1
	$1s_{1/2}$ (B)	58.4 ± 1.1	32 ± 1
Volkov *et al.*[c]	$1p_{1/2}$	29.8 ± 0.1	8.5 ± 1.1
$(p,2p)$ [18]	$1p_{3/2}$	34.7 ± 0.3	9.4 ± 1.2
	$1s_{1/2}$	53.6 ± 0.7	18.8 ± 1.4

[a]The values were obtained by fitting Maxwellian curves to the separation-energy spectra. We evaluated the listed widths from the values given in Ref. [13] (where the authors show the distances between the zero and the maximum of the Maxwellian curve) by regarding them as 3σ in a Gaussian function.
[b]Two results (A) and (B) were presented for the $1s_{1/2}$ orbital.
[c]Volkov *et al.* disentangled the $1p_{1/2}$- and $1p_{3/2}$-hole states by fitting the separation-energy spectra with some Gaussian functions.

all the strength uncertainties by a constant factor so that χ_ν^2 became 1, and so increased uncertainties in the parameters were obtained. The increased uncertainties involve the model uncertainties that originate in the inadequacy of the model, and they were defined as the total uncertainties. The uncertainties estimated without increase in the uncertainties in the strength data were defined as the statistical uncertainties.

The centroid energies (E_c) and widths (Γ) of the peaks for the $1s_{1/2}$- and $1p$-hole states were obtained as the parameters of the asymmetric Lorentzian function in the fit; they are listed in Table III with the results from previous experiments. The total uncertainties in the centroid energies and widths were estimated as mentioned before. The centroid energies of the $1p$- and $1s_{1/2}$-hole states are deduced to be 30.0 ± 0.4 and 49.6 ± 0.6 MeV, respectively.

The spectroscopic factors obtained by subtraction of the fitted four-body background are listed in Table IV, together with the total and statistical uncertainties. As stated in Sec. VI A, the uncertainty from the DWIA calculation was taken to be 17% and it was added in quadrature for the total uncertainty. In the spectroscopic factors without background subtraction in Table IV, the statistical uncertainties and the uncertainty from the DWIA calculation were added in quadrature to obtain the total uncertainties.

The spectroscopic factors deduced for the $1s_{1/2}$, $1p$, $2s_{1/2}$, and $1d_{3/2}$ orbitals are 78 ± 14%, 49 ± 10%, 60 ± 10%, and 78 ± 13% of the IPSM limits, respectively. However, the

TABLE IV. Spectroscopic factors relative to the IPSM limits for the orbitals in ^{40}Ca. They are obtained after subtraction of the background in the present study. The spectroscopic factors obtained without background subtraction are also listed. The first uncertainty is the total uncertainty and the second, in parentheses, is the statistical uncertainty included in the total. The statistical uncertainty and the uncertainty from the DWIA calculation are included in the total, and the model uncertainty is also included in the spectroscopic factors obtained after background subtraction.

	IPSM limit	Spectroscopic factor	
		Without background subtraction	Background subtracted
$1d_{3/2}$	4	$0.78 \pm 0.13(\pm 0.01)$	
$1f_{7/2}$	8	$0.097 \pm 0.017(\pm 0.005)$	
$2s_{1/2}$	2	$0.61 \pm 0.11(\pm 0.02)$	$0.60 \pm 0.10(\pm 0.02)$
$1d_{5/2}$	6	$1.33 \pm 0.23(\pm 0.05)$	$0.94 \pm 0.17(\pm 0.06)$
$1p$	6	$1.41 \pm 0.24(\pm 0.04)$	$0.49 \pm 0.10(\pm 0.06)$
$1s_{1/2}$	2	$1.12 \pm 0.19(\pm 0.03)$	$0.78 \pm 0.14(\pm 0.05)$

spectroscopic factor of $94 \pm 17\%$ for the $1d_{5/2}$ orbital is consistent with 100% within the uncertainty.

VII. DISCUSSION

The spectroscopic factors from the present result are compared with those obtained from the previous experiments in Table V. They are shown as ratios to the IPSM limits. The uncertainties are not given in the spectroscopic factors obtained by Mougey *et al.* [12]. The spectroscopic factors obtained from the $(e,e'p)$ experiment by Nakamura *et al.* are larger than the sum-rule limits except for the $1d_{5/2}$ orbital [15]. Their large spectroscopic factors for the $1p$ and $1s_{1/2}$ orbitals possibly suggest the inclusion of the continuum background in the higher-separation-energy region. The spectroscopic factors of 0.65 and 0.75 obtained by Mougey *et al.* [12] for the $2s_{1/2}$ and $1s_{1/2}$ orbitals are as low as the present results of 0.60 and 0.78, whereas the spectroscopic factor of 0.95 for the $1p$ orbital is much larger than the present result of 0.49. The centroid energy of 41 MeV obtained by Mougey *et al.* for the $1p$ orbital is much higher than the present result of 30.0 MeV, as seen in Table III. The larger spectroscopic factor and the higher centroid energy for the $1p$ orbital can possibly be explained by inclusion of the continuum background in

the $1p$-hole strengths in the higher-separation-energy region. It is also possible that the extremely high centroid energy of 77 MeV for the $1s_{1/2}$-hole state reported by Amaldi *et al.* [13] is due to the continuum background at higher separation energy. The centroid energies and widths of the $1s_{1/2}$- and $1p$-hole states obtained in the present results are close to the results from the $(p,2p)$ experiment at PNPI [18].

The present analysis depends on the background treatment. The spectroscopic factors obtained without background subtraction for the $1s_{1/2}$, $1p$, and $1d_{5/2}$ orbitals exceed the corresponding IPSM limits, as seen in Table IV. This indicates that the spectroscopic factors are greatly affected by the background estimation.

The background from the four-body final states in the high-missing-energy region in the ^{12}C$(e,e'p)$ reaction was investigated by Fissum *et al.* [45]. The measured separation-energy spectra were compared with calculation of the $(e,e'pp)$ and $(e,e'pn)$ reactions, included meson-exchange currents, isobar currents, central short-range correlations, and tensor medium-range correlations. However, the calculated cross section was smaller than the measured cross section by about 50% and did not clarify the total background components. The contribution of rescattering processes was studied by Cowley *et al.* [42]. It is remarkable that the calculated rescattering

TABLE V. Spectroscopic factors relative to the IPSM limits for the orbitals in ^{40}Ca obtained from previous experiments. For the present result, the first uncertainty is the total uncertainty, which includes the statistical uncertainty, the model uncertainty, and the uncertainty from the DWIA calculation, and the second, in parentheses, is the statistical uncertainty included in the total.

	IPSM limit	Present work	Mougey *et al.* [12][a]	Nakamura *et al.* [15][b]
$2s_{1/2}$	2	$0.60 \pm 0.10(\pm 0.02)$	0.65	1.0 ± 0.1
$1d$	10		0.77	
$1d_{3/2}$	4	$0.78 \pm 0.13(\pm 0.01)$		1.1 ± 0.4
$1d_{5/2}$	6	$0.94 \pm 0.17(\pm 0.06)$		0.78 ± 0.27
$1p$	6	$0.49 \pm 0.10(\pm 0.06)$	0.95	1.70 ± 0.15
$1s_{1/2}$	2	$0.78 \pm 0.14(\pm 0.05)$	0.75	2.60 ± 0.15 (A)
				1.9 ± 0.1 (B)

[a]The uncertainties were not given for the spectroscopic factors by Mougey *et al.*
[b]Two results (A) and (B) were presented for the $1s_{1/2}$ orbital.

TABLE VI. Spectroscopic factors relative to the IPSM limits for the orbitals in ^{40}Ca obtained from theoretical studies. For the present result, the first uncertainty is the total uncertainty, which includes the statistical uncertainty, the model uncertainty, and the uncertainty from the DWIA calculation, and the second, in parentheses, is the statistical uncertainty included in the total.

	IPSM limit	Present work	Fabrocini *et al.* [6]	Bisconti *et al.* [7]
$2s_{1/2}$	2	$0.60 \pm 0.10(\pm 0.02)$	0.86	0.87
$1d$	10		0.87	
$1d_{3/2}$	4	$0.78 \pm 0.13(\pm 0.01)$		0.85
$1d_{5/2}$	6	$0.94 \pm 0.17(\pm 0.06)$		0.86
$1p$	6	$0.49 \pm 0.10(\pm 0.06)$	0.58	
$1p_{1/2}$	2			0.81
$1p_{3/2}$	4			0.82
$1s_{1/2}$	2	$0.78 \pm 0.14(\pm 0.05)$	0.55	0.78

processes well reproduced the experimental coincidence spectra, especially in the kinematical region in which quasifree events were hardly expected. The rescattering process cannot be ignored in some kinematical regions in the coincidence measurement. Although the background components are still controversial, in the present study, we used the four-body phase space as the background-shape model, taking account of the four-body and rescattering processes. To compensate for the inadequacy of the model, the uncertainties in the deduced observables were estimated to include the model uncertainties, as previously mentioned.

The spectroscopic factors from the present result are compared with those from theoretical studies in Table VI. They are shown as ratios to the IPSM limits. The spectroscopic factors of 0.86 and 0.87 for the $2s_{1/2}$ orbital predicted by Fabrocini *et al.* [6] and Bisconti *et al.* [7] considerably exceed the present result of 0.60. This discrepancy could be explained by surface effects, which are not taken into account in their calculations. It is known theoretically that the surface effects reduce the spectroscopic factors for the orbitals near the Fermi level.

The spectroscopic factor of 0.49 for the $1p$ orbital is smaller than the predicted value of 0.58 by Fabrocini *et al.* in which the NN correlation significantly reduces the spectroscopic factors for the deeply bound orbitals. Both calculations, by Fabrocini *et al.* and Bisconti *et al.*, suggest that the spectroscopic factor decreases as the binding energy increases, although the values predicted by Bisconti *et al.* show a rather moderate reduction. Although the spectroscopic factor obtained for the $1s_{1/2}$ orbital is larger than that for the $1p$ orbital, it is still smaller than that for the $1d_{5/2}$ orbital. The present results support the conclusion that the NN correlations have a strong influence on the spectroscopic factors for deeply bound orbitals.

It is interesting that we observed a considerable reduction of the spectroscopic factor for the $1p$ orbital. However, the $1p_{1/2}$- and $1p_{3/2}$-hole states could not be separated in the present study because the DWIA calculation of the analyzing power was not fully reliable. It is important to be able to separate the hole states of the $1p_{1/2}$ and $1p_{3/2}$ orbitals, that is, the hole states of the $j_>$ and $j_<$ orbitals, by use of the analyzing power data, to obtain further information on the reduction of the spectroscopic factor for the deeply bound orbitals and to understand

NN correlations in atomic nuclei. Progress in the theoretical models that can explain the reduction of the analyzing power is expected.

A large reduction in single-particle strength has also been observed for the strongly bound valence neutrons near the Fermi surface in proton-rich unstable nuclei [46,47]. This reduction has been suggested to be due to the strong p-n interactions [48]. Although the nucleons in the $1p$ and $1s_{1/2}$ orbitals in ^{40}Ca are also strongly bound, these orbitals are far below the Fermi surface. Therefore, the mechanisms for reducing the spectroscopic factors for the $1p$ and $1s_{1/2}$ orbitals in ^{40}Ca may be expected to be different. We need further experimental study on the spectroscopic factors in other nuclei to clarify the NN correlations that contribute to the reduction of the spectroscopic factors for deeply bound orbitals.

VIII. SUMMARY

A ^{40}Ca$(\vec{p},2p)$ experiment was performed with a 392-MeV polarized proton beam to measure the recoil-momentum distributions of the cross section and the analyzing power in the separation-energy region of 0–89 MeV. The spectroscopic factors for the discrete peaks are consistent with those from $(e,e'p)$ and $(d,^3\text{He})$ reactions. It was confirmed that the DWIA calculation reproduces the dependence of the recoil momentum on the measured cross section reasonably well, but it systematically overestimates the analyzing power. The strength distributions for the deep-hole states were obtained from the MDA for each 2-MeV bin in the separation energy and were successfully separated from the continuum background by subtraction of a four-body background. The centroid energies and widths of the distributions were obtained for the $1p$ and $1s_{1/2}$ orbitals. The spectroscopic factors for the $1p$ and $1s_{1/2}$ orbitals were obtained as $49 \pm 10\%$ and $78 \pm 14\%$ of the IPSM limits, respectively, and it was indicated that the spectroscopic factors for the deeply bound orbitals are reduced owing to the NN correlations. Further development of the DWIA calculation of the analyzing power is expected to separate the hole states of the $1p_{1/2}$ and $1p_{3/2}$ orbitals and clarify the influence of the NN correlations on the spectroscopic factors.

ACKNOWLEDGMENTS

The experiment was performed under Program Nos. E168 and E217 at RCNP, Osaka University. The authors gratefully thank the RCNP cyclotron crew and technical staff for their support in providing a stable beam during the experiment and for the beam-time management. The authors would like to thank Professor A. Ozawa, Professor H. Okamura, and Professor A. Tamii for their support, allowing us to continue this research. The authors acknowledge Professor G. P. A Berg and Professor M. Fujiwara for valuable discussions about the present study. This research was supported in part by Grants-in-Aid for Scientific Research Nos. 20740120 and 21540303 from the Japan Ministry of Education, Sports, Culture, Science, and Technology.

[1] T. Otsuka, R. Fujimoto, Y. Utsuno, B. A. Brown, M. Honma, and T. Mizusaki, Phys. Rev. Lett. **87**, 082502 (2001).

[2] T. Otsuka, T. Suzuki, R. Fujimoto, H. Grawe, and Y. Akaishi, Phys. Rev. Lett. **95**, 232502 (2005).

[3] L. Lapikás, Nucl. Phys. A **553**, 297c (1993).

[4] G. J. Kramer, H. P. Blok, and L. Lapikás, Nucl. Phys. A **679**, 267 (2001).

[5] O. Benhar, A. Fabrocini, and S. Fantoni, Phys. Rev. C **41**, R24 (1990).

[6] A. Fabrocini and G. Co', Phys. Rev. C **63**, 044319 (2001).

[7] C. Bisconti, F. Arias de Saavedra, and G. Co', Phys. Rev. C **75**, 054302 (2007).

[8] S. Frullani and J. Mougey, Adv. Nucl. Phys. **14**, 1 (1984).

[9] P. Kitching, W. J. McDonald, Th. A. J. Maris, and C. A. Z. Vasconcellos, Adv. Nucl. Phys. **15**, 43 (1985).

[10] C. Mahaux and R. Sartor, Adv. Nucl. Phys. **20**, 1 (1991).

[11] J. J. Kelly, Adv. Nucl. Phys. **23**, 75 (1996).

[12] J. Mougey, M. Bernheim, A. Bussière, A. Gillebert, P. X. Hô, M. Priou, D. Royer, I. Sick, and G. J. Wagner, Nucl. Phys. A **262**, 461 (1976).

[13] U. Amaldi Jr., G. Campos Venuti, G. Cortellessa, E. de Sanctis, S. Frullani, R. Lombard, and P. Salvadori, Phys. Lett. **22**, 593 (1966).

[14] K. Nakamura, S. Hiramatsu, T. Kamae, H. Muramatsu, N. Izutsu, and Y. Watase, Phys. Rev. Lett. **33**, 853 (1974).

[15] K. Nakamura, S. Hiramatsu, T. Kamae, H. Muramatsu, N. Izutsu, and Y. Watase, Nucl. Phys. A **271**, 221 (1976).

[16] A. N. James, P. T. Andrews, P. Kirkby, and B. G. Lowe, Nucl. Phys. A **138**, 145 (1969).

[17] S. Kullander, F. Lemeilleur, P. U. Renberg, G. Landaud, J. Yonnet, B. Fagerström, A. Johansson, and G. Tibell, Nucl. Phys. A **173**, 357 (1971).

[18] S. S. Volkov et al., Sov. J. Nucl. Phys. **52**, 848 (1990) [Yad. Fiz. **52**, 1339 (1990)].

[19] A. A. Vorob'ev, Yu. V. Dotsenko, A. A. Lobodenko, O. V. Miklukho, I. I. Tkach, A. Yu. Tsaregorodtsev, and Yu. A. Shcheglov, Phys. At. Nucl. **58**, 1817 (1995) [Yad. Fiz. **58**, 1923 (1995)].

[20] I. Miura et al., in *Proceedings of the 13th International Conference on Cyclotrons and Their Applications, Vancouver, 1992*, edited by G. Cutte and M. K. Craddock (World Scientific, Singapore, 1993), p. 3.

[21] T. Wakasa et al., Nucl. Instrum. Methods Phys. Res. A **482**, 79 (2002).

[22] R. B. Firestone, S. Y. F. Chu, and C. M. Baglin, *Table of Isotopes* (John Wiley & Sons, New York, 1999), 8th ed., updated with CD-ROM.

[23] M. Fujiwara et al., Nucl. Instrum. Methods Phys. Res. A **422**, 484 (1999).

[24] N. Matsuoka, T. Noro, K. Sagara, S. Morinobu, A. Okihara, and K. Hatanaka, RCNP Annual Report, 1990, p. 235 (unpublished); RCNP Annual Report, 1991, p. 186 (unpublished).

[25] R. A. Arndt, W. J. Briscoe, I. I. Strakovsky, and R. L. Workman, Phys. Rev. C **76**, 025209 (2007); SAID Program, Center for Nuclear Studies, Data Analysis Center, http://gwdac.phys.gwu.edu.

[26] N. S. Chant and P. G. Roos, Phys. Rev. C **27**, 1060 (1983).

[27] R. A. Arndt, J. S. Hyslop III, and L. D. Roper, Phys. Rev. D **35**, 128 (1987).

[28] E. D. Cooper, S. Hama, B. C. Clark, and R. L. Mercer, Phys. Rev. C **47**, 297 (1993).

[29] L. R. B. Elton and A. Swift, Nucl. Phys. A **94**, 52 (1967).

[30] I. Angeli, At. Data Nucl. Data Tables **87**, 185 (2004).

[31] H. Sakaguchi, M. Nakamura, K. Hatanaka, A. Goto, T. Noro, F. Ohtani, H. Sakamoto, H. Ogawa, and S. Kobayashi, Phys. Rev. C **26**, 944 (1982).

[32] J. W. A. den Herder, H. P. Blok, E. Jans, P. H. M. Keizer, L. Lapikás, E. N. M. Quint, G. van der Steenhoven, and P. K. A. de Witt Huberts, Nucl. Phys. A **490**, 507 (1988).

[33] A. A. Cowley, G. J. Arendse, J. A. Stander, and W. A. Richter, Phys. Lett. B **359**, 300 (1995).

[34] S. Hama, B. C. Clark, E. D. Cooper, H. S. Sherif, and R. L. Mercer, Phys. Rev. C **41**, 2737 (1990).

[35] G. J. Kramer et al., Phys. Lett. B **227**, 199 (1989).

[36] P. Doll, G. J. Wagner, K. T. Knöpfle, and G. Mairle, Nucl. Phys. A **263**, 210 (1976).

[37] T. Noro et al., Phys. Rev. C **72**, 041602(R) (2005).

[38] C. A. Miller et al., Phys. Rev. C **57**, 1756 (1998).

[39] K. Hatanaka et al., Phys. Rev. Lett. **78**, 1014 (1997).

[40] O. V. Miklukho et al., Nucl. Phys. A **683**, 145 (2001).

[41] V. A. Andreev et al., Phys. Rev. C **69**, 024604 (2004).

[42] A. A. Cowley et al., Phys. Rev. C **57**, 3185 (1998).

[43] R. Sartor and C. Mahaux, Phys. Rev. C **21**, 2613 (1980).

[44] S. Terashima et al., Phys. Rev. C **77**, 024317 (2008).

[45] K. G. Fissum et al., Phys. Rev. C **70**, 034606 (2004).

[46] A. Gade et al., Phys. Rev. Lett. **93**, 042501 (2004).

[47] A. Gade et al., Phys. Rev. C **77**, 044306 (2008).

[48] R. J. Charity, L. G. Sobotka, and W. H. Dickhoff, Phys. Rev. Lett. **97**, 162503 (2006).